

Reconstructing External Force on the Circumferential Body of Continuum Robot With Embedded Proprioceptive Sensors

Qingxiang Zhao , Jiewen Lai , *Student Member, IEEE*, and Henry K. Chu , *Member, IEEE*

Abstract—The compliance of continuum robot poses difficulty in designing the controller, as the robot does not have position encoder and could be subject to uncertain external force (UEF). The former can be resolved through external sensors, while the latter issue still needs further investigation. This article presents a novel robot design that embeds eGaN sensors into the soft material, and the elongation in the robot chamber can lead to different changes in resistance values. The sensors act as a proprioceptive mechanism to sense the presence of the UEF. To locate the UEF, the robot surface is divided into multiple regions, and the column and row positions with the force can be solved using Hidden Markov Model and regularization algorithm. Through the virtual work principle, the force magnitude can be also evaluated. Experimental results confirm that, with possible four columns and five rows, the accuracy of finding the actual column and row positions are, respectively, 97% and 98.5%. The mean error in evaluating the tip position and the force magnitude is about 4 mm and 0.23 N. This article offers a new approach to obtain the information of the UEF, allowing continuum robots to work in a constrained environment.

Index Terms—Continuum robot, embedded flexible sensors, external force reconstruction, hidden Markov model, regularization, virtual work principle.

I. INTRODUCTION

THE emergence of continuum robot has endowed robotics with a novel research branch. Some obvious merits, such as hyper redundancy, high compliance, and cost effectiveness over rigid robot arms, make it widely applied in surgery [1], [2], search and rescue [3], [4], and pick-place tasks [5]. Research on continuum robots in recent decades includes versatile actuation mechanisms [6], [7], advanced sensors, mechanical design and control models [5]. However, continuum robot also comes with challenges. Specifically, it is difficult to pinpoint the location

Manuscript received April 19, 2021; revised August 3, 2021 and September 28, 2021; accepted November 9, 2021. Date of publication December 2, 2021; date of current version July 8, 2022. This work was supported in part by the Grant 4-RKDQ of The Hong Kong Polytechnic University. (*Corresponding author: Henry K. Chu*)

The authors are with the Department of Mechanical Engineering, The Hong Kong Polytechnic University, Hong Kong (e-mail: qingxiang.zhao@connect.polyu.hk; jw.lai@connect.polyu.hk; henry.chu@polyu.edu.hk).

This article has supplementary material provided by the authors and color versions of one or more figures available at <https://doi.org/10.1109/TIE.2021.3130326>.

Digital Object Identifier 10.1109/TIE.2021.3130326

and estimate the magnitude of an external force (EF) acting on a continuum robot in a constrained environment. The lack of information about the uncertain external force (UEF) can cause different degrees of changes on the shape of a soft manipulator, posing difficulty to design a proper control scheme for the robot.

Finding the location of the force can help users (e.g., surgeons) to better interact with the ambient environment, and adjust the actuation inputs accordingly to compensate the load effect. To this end, sensors are indispensable. Externally located camera [8] is a good option to directly monitor the robot as well as the surrounding obstacles, but occlusion could be a problem in some scenarios. Therefore, research towards proprioceptive sensing has been developed. Examples of existing works include employing fiber bragg grating (FBG) [9], electromagnetic (EM) [10], Hall effect [11], stretchable optical waveguides [12], and color-related sensors [13] to achieve shape sensing and force sensing for soft robots, where the signal outputs correspond to the change in the robot shape. Similarly, there are some limitations in these sensing mechanisms. For example, FBG is not cost-friendly and has limited bending flexibility. EM and Hall-effect sensors are sensitive to the surrounding magnetic field presented in the environment. Optical waveguides and color sensors need complicated fabrication procedures for sensor integration and are not feasible for small-sized robots. Recently, intrinsic properties of the robot have also been used for self-sensing. The shape of a dielectric actuated elastomer [14] is related to its capacitance values, and measuring the voltage and the current value can help to derive external force from the change in the shape accordingly. The signals provided to the pneumatic chamber is another useful information, acoustic or pressure signal can be collected to estimate the robot shape [15], [16]. While the overall shape is known, the effect from the external force is hard to be evaluated separately from the actuation inputs. In recent decades, the development of flexible electronics paves a way of compact and soft internal sensors for soft robots. Flexible and conductive materials, like eGaN (eutectic gallium indium, a liquid alloy) [17], [18] and ionic solution [19], can be integrated into soft nonconductive silicone to form compliant skin sensors, which are employed to sense the stress in minimally invasive surgery [20], strain [21], and shape [22] for robots.

In addition to sensors, establishing a proper model of the continuum robot is also essential for control and force estimation. Piecewise constant curvature (PCC) approximation [23] regards the shape of a single continuum robot as an arch, which

is determined by the length of each actuation chamber, but the direction angle and the bending angle of the PCC model are jointly affected by actuators and the external forces. The other stream of modelling is to assume a flexible manipulator as an Euler–Bernoulli beam [24] or a Kirchhoff elastic rod [4]. Therefore, the kinematics can be obtained by solving the displacement of robot's backbone with all the acting forces, but an UEF can act at any position and any direction. In the velocity domain, Jacobian matrix maps between the velocities of actuators and the end effector [25], so that in a short interval, the position change of the tip can be solved using the change of actuation configuration. Analytical models are problematic in an unstructured environment due to the uncertainty of the UEF. Thus, models considering the environmental information are likely to achieve higher precision so that machine learning [26] and fuzzy control models [27] were investigated. Building machine learning models is time-consuming and the environmental information in model training is often static, which is not consistent with dynamic UEF, and fuzzy control methods aim to bring the robot tip to a desired position, which may not be attainable in some applications. Thereby, accurately estimating the UEF faced by soft robots not only benefits handlers but also contributes to building better control schemes. For instance, in [14], a feedback control scheme was proposed based on the estimated force. The shape of an elastomer was modeled by the actuation force and the external force, so that the system can intelligently avoid obstacles and adjust the controller outputs. In [28], contact detection was realized along a pneumatic-driven flexible manipulator. Similar to kinematics, estimating the UEF can be an inverse process when the manipulator is assumed as a Cosserat Rod [29], where the actuation configuration and the robot shape were both known. Nevertheless, existing works only considered the force applied at the tip, or sense the deformation type of the robot caused by an UEF [30]. The essential difficulty of estimating the UEF has twofold: 1) UEF can fall into any position along the manipulator, and 2) the direction of the UEF at an action point has three components (x, y, z); thus, its magnitude varies irregularly. To find the location of the force acting arbitrarily on the body, *Qiao et al.* [31] and *Venkiteswaran et al.* [32] combined FBG signals with Cosserat model and Pseudo Rigid Body model, respectively, to solve the position information. However, these approaches are computationally intensive. Alternatively, an array of force sensors can be wrapped along the surface of the continuum robot. This method, however, requires many sensors in order to cover the entire surface. The prevalence of Deep Learning provides a novel method [33]; for example, in [34] and [35], a *Deep-Table* frame and RNN model were, respectively, applied to estimate loads of a robot arm and to estimate hard inclusions of soft tissue. Most of existing works just focused on some specific small areas of the elastomer in estimating the UEF, or only the posture of the soft robot [36], and the motion of the robot is only planar (2-D) [37].

In contrast, this article aims to find the external force acting on the circumferential body of a soft manipulator, including the acting position and the magnitude. That is a relatively bigger area and the information of the estimated EF is more complete. The contribution includes the following.

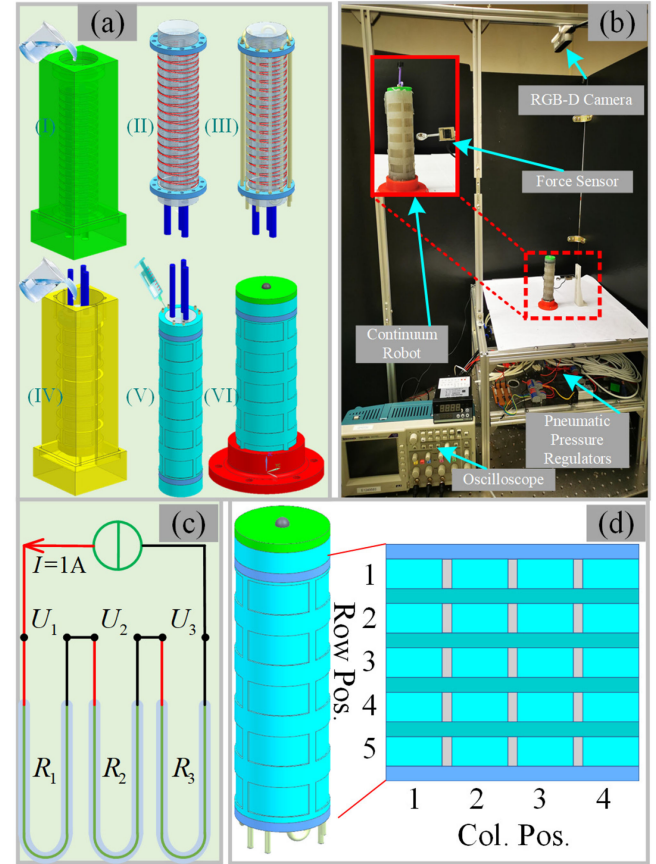


Fig. 1. (a) Fabrication of the manipulator. (b) System setup. (c) Circuit of electronic resistance measurement. (d) Schematic view of the circumferential view of the soft manipulator.

- 1) A model-free approach is proposed to determine the presence of an EF using the signals from embedded soft sensors.
- 2) The surface of the robot is considered as a 2-D map with multiple grids, and a probability approach is used to find the likelihood of the column position. After this, the row position and the corresponding magnitude are estimated by virtual work principle.

The rest of this article is organized as follows. Section II described how we fabricated an eGaIn sensor and integrated it into the soft robot arm. In Section III, we detailed the methodology to estimate a single external force. Experiments were conducted to validate the proposed method, as detailed in Section IV. Finally, Section V concludes this article.

II. SYSTEM SETUP AND CONFIGURATION

Silicone molding technology was employed to fabricate a soft manipulator, and the fabrication procedures are illustrated in Fig. 1(a). Silicone rubber (E605, Hong Yejie, Shenzhen, China) was poured into a 3D-printed mold [see Fig. 1(a)-(I)] to form the inner component of the manipulator, which was then wrapped by a Nylon thread to limit the radial expansion once the chambers are pressurized. Two helical grooves were designed in the mold, preventing the wrapped threads from

slipping during the operation [see Fig. 1(a)-(II)]. Next, the inner component was secured by two disks at the two ends, and three insulated thin silicone tubes (OD:1 mm, ID:0.5 mm), which serve as the channels for eGaIn, were connected to the two disks [see Fig. 1(a)-(III)]. Then, the entire component was placed into another mold to form the outer layer [see Fig. 1(a)-(IV)]. After demolding, an outer layer surface consisting of twenty concave faces (4 columns and 5 rows) along the manipulator were obtained. Then, eGaIn was injected into the three thin tubes [see Fig. 1(a)-(V)], where the elongation of the tube will simultaneously decrease its cross-sectional area, such that the electronic-resistance change of eGaIn sensors ($R = \rho \frac{l}{S}$) can reflect the deformation of the manipulator. The three sensors are connected in series and a constant current power source of 1 A is then supplied, as shown in Fig. 1(c). The voltage difference across each sensor is measured via an oscilloscope (Tektronik TBS 1064), which converts the resistance change into voltage signal. Finally, three supporting steel bars [marked in blue in Fig. 1(a)] that are located 120° apart were removed, providing the space as the chambers for actuation. Two rings were then glued at the two ends, allowing a marker to be placed at the top for tip position evaluation and mounting at the bottom [see Fig. 1(a)-(V)]. The region that an UEF is likely to present along the circumferential body can be indexed by the column and the row numbers radially. A schematic view of the circumferential surface is shown in Fig. 1(d)-(right), and the problem lies in accurately finding the two positions to pinpoint the external force and then to estimate its magnitude, with an assumption that the UEF is always pointing towards the backbone of the manipulator.

To actuate this soft manipulator, the three chambers were connected to three pneumatic pressure regulators (ITV-0030, SMC), and the pressurized air can be controlled with an accuracy of 0.01 bar. The manipulator was mounted vertically in an aluminium frame, and a calibrated RGB-D camera (Realsense D415, Intel) was set up at the top of the frame to sample the true position at the tip, as illustrated in Fig. 1(b). A single-axis force sensor (ZNLBS-VII, Zhongnuochuanli, Bengbu, Anhui, China, range: $[-5, 5]N$) was placed next to the manipulator, providing the true external force magnitude for validation. A control interface was developed using MATLAB 2019b.

III. UEF LOCALIZATION AND MAGNITUDE ESTIMATION

The tip position is the combined result from the actuation inputs and the external force, as shown in Fig. 2(a), where the shape of the manipulator at step k can be deemed as an arch defined by three parameters: the direction angle ψ_k , the bending angle θ_k , and the bending radius R_k . All of them can be solved using (A1) (equation in Appendix) if the tip position $P_k(x_k, y_k, z_k)$ can be obtained. Since the three eGaIn sensors are mounted adjacent to the three chambers respectively, the sensor readings directly correlate with the chamber length, so that the real-time tip position both in load-free and load conditions can be computed based on the sensor readings S_k . Namely, the true tip position P_k can be mapped via S_k .

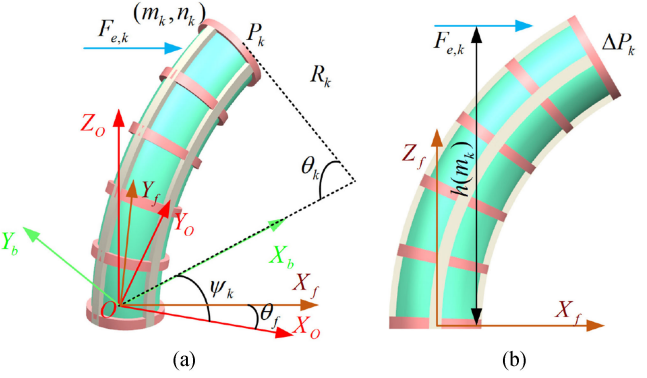


Fig. 2. Illustration of deformed flexible arm. (a) Coordinate frames. (b) Tip position in $X_f O Z_f$ only due to an external force.

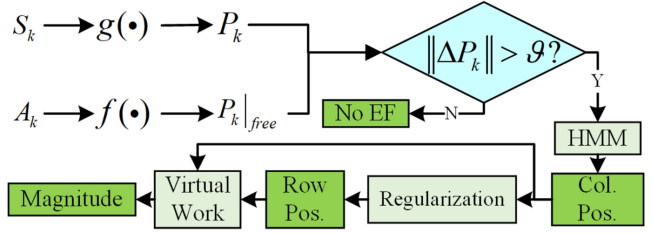


Fig. 3. Flowchart of external force estimation.

In load-free condition, the tip position can be regarded as solely depending on actuation inputs A_k , which means that tip position $P_k|_{\text{free}}$ can be solved just using A_k . In contrast, as shown in Fig. 2(b), an external force $F_{e,k}$ causes the true tip position P_k to deviate from the theoretical load-free value $P_k|_{\text{free}}$. When the external load is present, the position deviation $\Delta P_k = P_k - P_k|_{\text{free}}$ in the tip position is large due to $F_{e,k}$. Therefore, by knowing the current actuation inputs A_k , the deviation can imply whether or not $F_{e,k}$ is present.

The evaluation method consists of three parts. First, the models to find $P_k|_{\text{free}}$ and P_k are constructed using Neural Network. Then, the column position of an UEF is estimated with HMM. Finally, the row position and the magnitude are calculated using the principle of virtual work. The overall framework is illustrated in Fig. 3.

A. Tip Position Prediction

Sensor readings are highly and directly related to the shape and the tip position, such that a mapping $g(\cdot)$ between P_k and S_k : $P_k(x_k, y_k, z_k) = g(S_k)$ can be built to form a proprioceptive sensing mechanism, both in load and load-free conditions. Fabrication imperfection and uncertainty of the EF increase the difficulty to find an analytical mapping, so using data-driven method to build Neural Network model provides a feasible alternative. Similarly, $P_k|_{\text{free}}$ is also solved, which is $P_k|_{\text{free}} = f(A_k)$. Since the input data and the position data do not vary significantly over time, an embedded dimension d is considered to estimate the position using last d records of data, and the two mappings are

updated as

$$\begin{cases} P_k|_{\text{free}} = f(A_{k-d:k}) \\ P_k(x_k, y_k, z_k) = g(S_{k-d:k}) \end{cases}. \quad (1)$$

Two multilayer perceptron (MLP) Neural Networks are, respectively, constructed to find $f(\cdot)$ and $g(\cdot)$. We set the embedded dimension $d = 5$. The output layer and input layer of the two models has 3 and 15 nodes, respectively, and the activation functions in hidden layer and output layer are “Sigmoid” ($y = \frac{1}{1+e^{-x}}$) and “ReLU” ($y = \max(0, x)$), respectively. A threshold ϑ is set to account for model error. Through comparing between ΔP_k and ϑ , UEF is detected as

$$\begin{cases} \text{UEF} & \|\Delta P_k\| \geq \vartheta \\ \text{Load Free} & \text{else.} \end{cases} \quad (2)$$

B. Column Position Estimation Towards UEF Via HMM

After identifying the existence of an UEF, its position can be estimated based on the tip position deviation ΔP_k . As Figs. 2(b) and 1(d) illustrate, there are 20 regions where an UEF is likely to present, one of which is denoted by (m, n) ($m \in [1, 5]$, $n \in [1, 4]$ are row position and column position, respectively). We first solve n_k because it is involved in the deviation direction of the tip, and the row position m_k as well as the magnitude affects deviation degree (i.e. bending angle). In the robot system, only A_k , ΔP_k , and S_k are known, which refers to observation data, and the column position n_k is hidden. Because of the uncertainty of the EF and slow motion of the robot, the state is only mapped with the current observation data. This satisfies the property of HMM, inspiring us to estimate the hidden state n_k by it. The observation sequence $O = (o_1, \dots, o_k)$ and a well learned HMM λ are employed to find the column position

$$\hat{n}_k = \arg \max_{1 \leq i \leq 5} \Pr(n_k = i | \lambda, O) \quad (3)$$

where $\hat{n}_k = 5$ means no UEF, and the observation data o_k depends on the actuation inputs and the position deviation: $o_k^{1 \times 6} = \{A_k^{1 \times 3}, \Delta P_k^{1 \times 3}\}$. To reduce the unit discrepancy, the actuation inputs are normalized with [0,1] and further expressed as

$$\begin{aligned} o_k(l) &= \begin{cases} -1 & A_k(l) \in [0.0, 0.33] \\ 0 & A_k(l) \in [0.34, 0.66] \\ 1 & A_k(l) \in [0.67, 1] \end{cases} \\ o_k(l) &= \begin{cases} 0 & \|\Delta P_k(l-3)\| \leq \xi \\ \text{sgn}(\Delta P_k(l-3)) & \text{else} \end{cases} \quad (4) \end{aligned}$$

where $\xi = 3$ mm is a threshold considering the measurement error. The hidden state of our HMM is the column position n_k and the state transition probability between two continuous steps i and j is: $a_{ij} = \Pr(n_{k+1} = j | n_k = i)$. In addition, the emission probability is defined as: $b_j(o_k) = \Pr(o_k | n_k = j)$. As a result, there are possibly in total $N = 3^6$ different observation data, which is difficult to manifest their corresponding emission probability. This issue was previously tackled by multivariate Gaussian distribution [38], requiring a large amount of data to find the mean value and variance. Therefore, K-means algorithm is employed to reduce the dimension of the observation data, and

the observation data are classified into one hundred categories (input one observation data with 6-D to get 1-D). The observation data o_k is updated to $v_k: v_k^{1 \times 1} \leftarrow K\text{means}(o_k^{1 \times 6})$, and the observation sequence O is: $\{v_1, \dots, v_k\}$.

Initially, the state transition probability is assumed as an uniform distribution, so that the initial probability for each hidden state is $\pi_i = \frac{1}{5}$. Now, this HMM is defined as: $\lambda = \{\pi, a_{ij}, b_j(v_k)\}$. With Bayesian's rule, (3) is updated to

$$\hat{n}_k = \arg \max_{1 \leq i \leq 5} \frac{\Pr(n_k = i, O | \lambda)}{\Pr(O | \lambda)}. \quad (5)$$

In order to calculate $\Pr(O | \lambda)$, forward and backward probability are defined as

$$\begin{aligned} \alpha_k(i) &= \Pr(v_1, \dots, v_k, n_k = i | \lambda) \\ \beta_k(i) &= \Pr(v_k, \dots, v_T | n_k = i, \lambda) \end{aligned} \quad (6)$$

so $\Pr(O | \lambda)$ can be further calculated by

$$\Pr(O | \lambda) = \sum_{i=1}^5 \sum_{j=1}^5 \alpha_k(i) a_{ij} b_j(v_{t+1}) \beta_{t+1}(j). \quad (7)$$

Let $\gamma_k(i)$ denotes the probability of hidden state i with knowing λ and O at step k , and $\xi_k(i, j)$ represents the probability of hidden state j at step $(k+1)$ if the hidden state is i at step k , both of which are then denoted as

$$\begin{aligned} \gamma_k(i) &= \Pr(n_k = i | O, \lambda) = \frac{\alpha_k(i) \beta_k(j)}{\sum_{j=1}^5 \alpha_k(i) \beta_k(j)} \\ \xi_k(i, j) &= \Pr(n_k = i, n_{k+1} = j | O, \lambda) \\ &= \frac{\alpha_k(i) a_{ij} b_j(o_{k+1}) \beta_{k+1}(j)}{\sum_{i=1}^5 \sum_{j=1}^5 \alpha_k(i) a_{ij} b_j(o_{k+1}) \beta_{k+1}(j)}. \end{aligned} \quad (8)$$

To obtain a well-learned HMM model, T sets of data including the observation data and the column position are collected, and the Baum–Welch algorithm is employed. Finally, the parameters of λ are learned via

$$a_{ij}^{n+1} = \frac{\sum_{k=1}^{T-1} \xi_k(i, j)}{\sum_{k=1}^{T-1} \gamma_k(i, j)}, b_j(k)^{n+1} = \frac{\sum_{k=1}^T \gamma_k(j)}{\sum_{k=1}^T \gamma_k(j)}. \quad (9)$$

The initial probability is $\pi_i^{n+1} = \gamma_1(j)$. After iterations, we can get: $\lambda^{(n+1)} = \{\pi^{(n+1)}, a_{ij}^{(n+1)}, b_j^{(n+1)}(n_k)\}$, so the estimated column position at step k is

$$\hat{n}_k = \arg \max_{1 \leq i \leq 5} [\gamma_k(i)]. \quad (10)$$

C. Row Position and Magnitude Estimation

After estimating the column position of a single EF ($\hat{n}_k \neq 5$), the algorithm still needs to find the row position m_k , which is related to the moment that the robot is experiencing. The robot can reach a static equilibrium with a tip position after

all the acting forces are in balance, and the equilibrium can be established by virtual work principle as

$$\delta W = \delta W_g + \delta W_{el} + \delta W_{ac} + \delta W_e = 0 \quad (11)$$

where δW_g , δW_{el} , δW_{ac} , and δW_e , respectively, denote the virtual work of gravity, elastic force from the robot itself, the actuators, and the external force. The centroid C_k locates at the center of the robot backbone, as calculated using (A3) in Appendix, so $\delta W_g = G \cdot \delta C_k$. The length of each chamber is solved using (A2) and the elongation of each chamber is: $\Delta l_{k,i} = l_{k,i} - l$. Therefore, δW_{el} can be calculated by: $\delta W_{el} = \sum_{i=1}^3 \frac{1}{3} EI \Delta l_{k,i}^2$, where E is the Young's Modulus and I is the inertial moment. Similarly, the virtual work of the actuators is the accumulation of the three chambers: $\delta W_{ac} = \sum_{i=1}^3 A_k(i) \pi r_c^2 \Delta l_{k,i}$ (r_c is the radius of the chamber). All virtual work can be expressed as functions in term of bending angle θ_k . The external force can be present in any position of the 20 areas, so $\delta W_e = F_e \delta_e$, where δ_e is involved in $\delta \theta_k$ and the row position \hat{m}_k . Although all of them can be solved, (11) includes both the magnitude and the row position of an external force. It would be difficult to evaluate them simultaneously. Considering that the tip position deviation is purely caused by the external force, we can use ΔP_k to establish another mapping: $\Delta P_k \leftarrow (F_{e,k}, m_k)$.

The flexible manipulator is assumed as a system and the tip position P_k reflects its system response influenced by the external force and the actuation inputs, which is expressed as

$$P_k = H(A_k)A_k + H_e(m_k)F_{e,k} + Q \quad (12)$$

where $H(A_k) \in R^{3 \times 3}$ is a system matrix relating between the tip position (system response) and the actuator inputs (i.e., $f(\cdot)$), and $H_e(m_k)$ is a matrix involved in the position of the external force $F_{e,k}$. The tip position change caused by an UEF at a certain row position, namely $H_e(m_k)F_{e,k}$, is calculated using (A4). Since we have found the column position in the previous section, only m_k and $F_{e,k}$ are unknown in this equation. Q is the Gaussian white noise indicating the systematic error. $H(A_k)A_k$ denotes the pure systematic response from the actuators, so (12) is updated as

$$\Delta P_k = H_e(m_k)F_{e,k} + Q \quad (13)$$

ΔP_k is the pure systematic response due to $F_{e,k}$. Therefore, the row position of $F_{e,k}$ can be solved by

$$\hat{m}_k = \arg \min_{m_k} \|\Delta P_k - H_e(m_k)F_{e,k}\|_2^2. \quad (14)$$

However, finding the optimal solution is not easy with many local minima. Since the equation may not yield to the global minima due to the noise and local minima, a regularization factor is also added to the equation to ensure convergence

$$\arg \min_{m_k} (\sqrt{\|\Delta P_k - H_e(m_k)F_{e,k}\|_2^2} + \chi \sqrt{\|F_{e,k}\|_2^2}) \quad (15)$$

where χ is a regularization parameter. After finding the row position m_k , the magnitude of the external force can be accordingly solved via (13). However, the value of χ is really important for the results, and setting a proper χ requires delicate calculation. We employ gradient descent algorithm to set different values

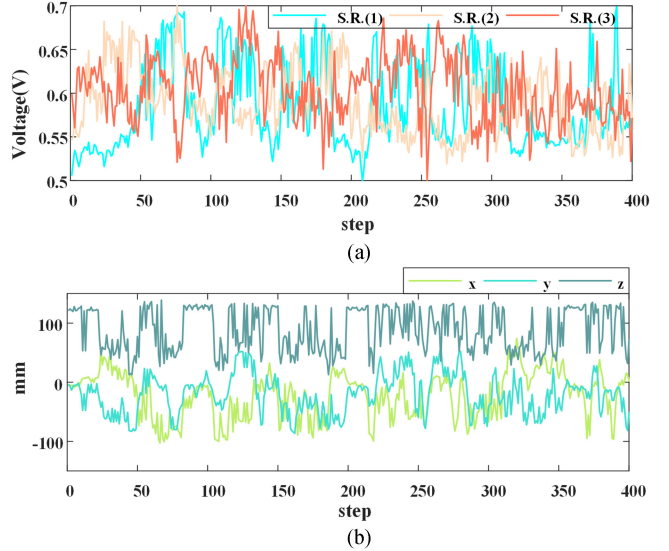


Fig. 4. Fundamental test about the experimental setup. (a) Sensor readings. (b) (x, y, z) of the tip position in task space.

of χ to address the issue. In virtual work principle, the ideal value of δW is close to zero, but an improper χ may lead to a large error in $\delta W(\chi)$. As a result, an iteration process was employed to update χ such that $\delta W(\chi)$ can converge to an value within an user-defined threshold ς : $\hat{\chi} = \chi - \eta \delta W(\chi)$, where η is the learning rate. When the algorithm finds the most possible position of the external force with different χ , the magnitude can also be calculated via (13).

IV. EXPERIMENTAL VALIDATION

Experiments were conducted to test the performance of the sensors and each module of the algorithm.

A. Sensor Performance

Robot was commanded to explore its task space by randomly setting the air pressure of each chamber for 2000 times in load-free condition, where the pressure was increased or decreased 0.05 bar, or kept unchanged between steps, and the tip varied continuously. After the robot became stable after each step, the sensor readings were collected ten times to store their mean value. Fig. 4 shows 400 sets of data, indicating the sensors are capable of outputting different values based on the shape of the robot. The data were also used to train the two tip position sensing models. The sensors are further examined about robustness and temperature-resistance ability.

1) Robustness

First, only one chamber was actuated in load-free state for ten times using same actuation inputs: varied from 0 to 0.6 bar with an increment of 0.05 bar (13 actuation inputs in total, in room temperature 25°C), and the eGaN sensor beside the chamber directly detected the length change. Fig. 5 shows the variation of the sensor reading, from which the maximum variance with 0.016 V appears at 0.4 bar. This indicates the robustness of the sensor and can clearly map the shape change of the robot.

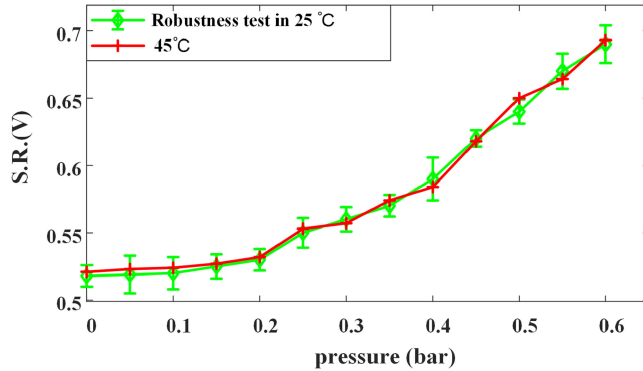


Fig. 5. Performance of robustness and in different temperature.

TABLE I
DATA AND RESULTS FOR THE TIP POSITION SENSING MODELS
("Y": USE THE DATA, AND "N": NOT USE.)

Training data		
load free	20g weight at tip	20g weight at mid.
2000 sets	1000 sets	1000 sets
$f(\cdot)$	Y	N
$g(\cdot)$	Y	Y
Testing data (max. err./ mean err. unit: mm)		
load free	dual 20g weight	30g weight at tip
100 sets	(tip. and mid.) 100 sets	100 sets
$f(\cdot)$	Y (3.98/3.19)	N
$g(\cdot)$	Y (3.87/3.26)	Y (3.94/3.31)
		Y (4.13/3.45)

2) Performance in different temperatures

In addition, the manipulator was heat in an oven with 45°C for one hour, and remount back to the platform for another testing. Using the same actuation inputs, we obtained similar sensor readings data, as shown in Fig. 5. The data are almost similar to that obtained in 25°C , showing the eGaIn can work robustly in common temperature range.

B. Results of Tip Position Proprioceptive Mechanism

The position deviation ΔP_k is one important input data for HMM, so its accuracy is highly involved in the UEF estimation result. To train $f(\cdot)$, the data collected in Section IV-A (load-free condition) was used. To mimic the robot operation under a load (i.e., with EF), a weight with 20 g was hung at the robot tip and at the middle part, and random actuation inputs were commanded to robot to reach another 100 new positions, respectively. The true tip position was collected using the RGB-D camera. The data for training and testing the two models is listed in Table I. In training, the maximum iteration in each model was set to 1000, and the learning rate was 0.1.

In terms of validation, one hundred new data of random actuation inputs were commanded to the robot in load-free condition, covering almost the entire task space of the tip. The ground truth was also collected by the RGB-D camera for comparison. Fig. 6(a) shows the comparison between the actual tip position and the values predicted by $f(\cdot)$ in load-free condition. The maximum error between the predicted and the actual values in all the 100 steps is 3.98 mm, while the mean position error is 3.19 mm.

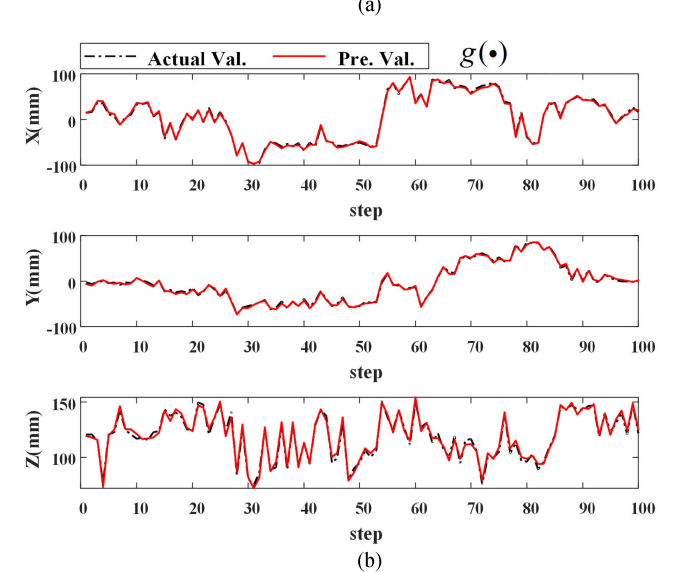
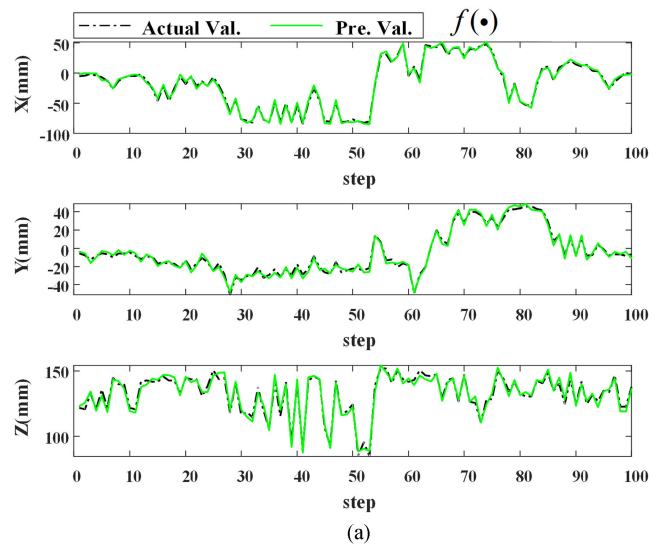


Fig. 6. Validation towards $f(\cdot)$ and $g(\cdot)$. (a) Load-free testing. (b) Load (dual 20 g weights added at the tip and middle area) condition testing.

To test the performance of $g(\cdot)$, in addition to the new 100 data for $f(\cdot)$, 100 sets of data with two 20 g loads at the tip and in the middle, and 100 sets of data with a 30 g weight at the tip were considered, as listed in Table I-Testing data. The multiload case was not included in the training data, and the results demonstrate the predicted tip position is generally accurate compared with the ground truth. The position value on each axis for the 100 data (two 20 g weights) is plotted in Fig. 6. As Fig. 6(a) shows, $f(\cdot)$ can properly predict the tip in load-free scenario, and no significant error was observed as compared with the measurement from RGB-D. Similarly, even with the unseen multiple loads, $g(\cdot)$ can also properly predict the tip, as shown in Fig. 6(b). To ensure that ΔP_k can effectively detect the presence of UEF in all three scenarios: no load, load at the tip, and multiple loads, three random actuation inputs were selected and the predicted from $f(\cdot)$ and $g(\cdot)$ under the three scenarios are summarized in Table II. Results confirm that ΔP_k is small when there is no load and is large in the presence of loads. Based

TABLE II

PREDICTED TIP POSITION UNDER THE SAME ACTUATION INPUTS
(Up: $p_k|_{\text{FREE}}$, Mid: P_k , Bottom: ΔP_k , Unit: mm)

Act. Inputs (bar)	load free	dual 20g weights	30g weight at tip.
(0,1,0,2,0.5)	(19.7,-2.9,150.7)	(19.7,-2.9,150.7)	(19.7,-2.9,150.7)
	(20.8,-3.4,151.6)	(40.4,92.2,83.5)	(34.5,-84.1,100.2)
	1.5	118.3	96.8
(0.4,0,4,0)	(-45.4,29.9,88.5)	(-45.4,29.9,88.5)	(-45.4,29.9,88.5)
	(-46.6,30.2,89.2)	(-74.1,-35.5,132.6)	(-64.7,16.5,147.8)
	1.4	83.9	63.8
(0.6,0,2,0.3)	(-101.8,42.8,102.7)	(-101.8,42.8,102.7)	(-101.8,42.75,102.7)
	(-102.3,43.6,104.8)	(-108.4,-58.7,56.6)	(-122.2,21.1,67.2)
	2.4	111.6	46.3

on the results, the threshold ϑ used to determine the force for ΔP_k was set to 5 mm.

C. Testing on Column Position Estimation

The abovementioned experiments validated the performance of the sensors and the mechanism to sense the presence of an UEF. Once the force is detected, HMM can be employed to find the column position accordingly. To examine the model, 500 sets of data were first prepared for training and another 100 sets were prepared for validation. The robot was randomly moved to a new location, and a metal bar was used to poke on the surface and exerted a force onto the robot. The location where the bar poked at (i.e., the column and row positions) was randomly selected. At some steps, no force was exerted onto the robot to also include the no-load case to the data. The learned state transition probability matrix is illustrated in Fig. 7(a). Validation using the 100 sets of data is summarized in Fig. 7(c). It can be observed that HMM can predict the column position properly and only three of the estimated results (the 4th, 42th, and 88th) did not match, reaching an accuracy of 97%. To better show the accuracy of the model, a simpler prediction method, inspired by [39], to predict the force direction, which is based on the change in tip position (x, y) due to the force, was considered for comparison, and the algorithm is listed as

$$\hat{n}_k = \begin{cases} 1 & \Delta P_k(1) < 0, \Delta P_k(2) < 0 \\ 2 & \Delta P_k(1) > 0, \Delta P_k(2) < 0 \\ 3 & \Delta P_k(1) > 0, \Delta P_k(2) > 0 \\ 4 & \Delta P_k(1) < 0, \Delta P_k(2) > 0 \\ \text{free} & \|\Delta P_k\| < \vartheta \end{cases} \quad (16)$$

The results of this method is also shown in Fig. 7(c) (threshold). While the column position can still be predicted, but the accuracy is only 90%. In addition, this simpler prediction method can only work with 4 quadrants, and the HMM method is needed for higher column resolution.

In addition to pushing force, tension was also considered to test the trained HMM. Four threads were secured to the surface of robot to generate pulling force at the four columns, as shown in Fig. 7(b)-(Right). In total, 100 sets of random actuation inputs and random pulling were prepared and the results are shown in Fig. 7(d). Both HMM and the simpler prediction methods can still predict the column position, the accuracy using HMM (96%) remains higher than the simpler method (91%). A video showing

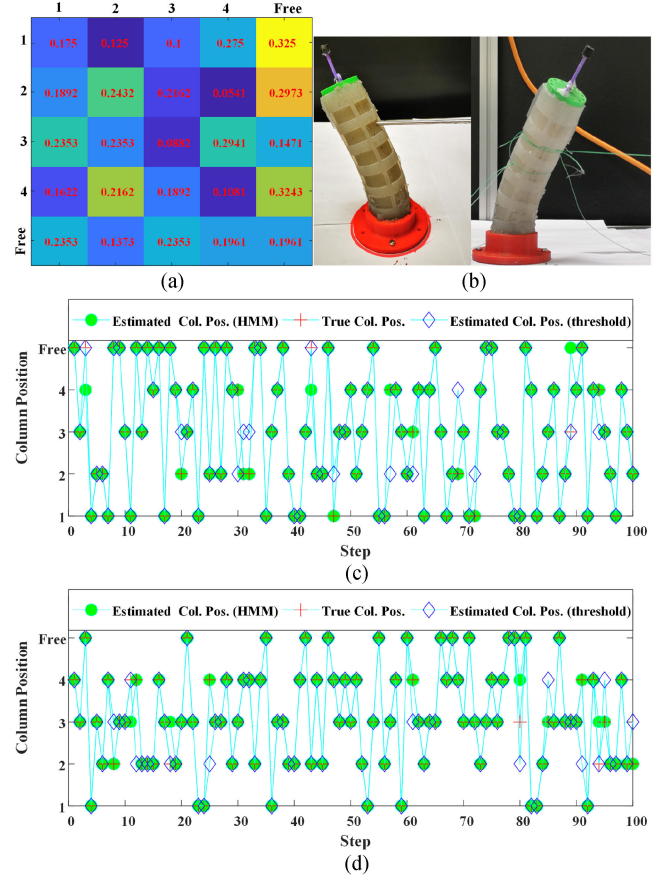


Fig. 7. (a) State transition probability. (b) Snapshots robot experiencing different EF. (c) and (d) Column position estimation results when robot was excited by a bar (pushing force) and thread (tension), respectively.

TABLE III
MATERIAL PROPERTIES

Property	Value	Property	Value
E Young's Modulus	2.7 MPa	r_c Chamber Radius	2 mm
ρ Density	1.07 (g/cm ³)	l Backbone Length	120 mm
r Distribution Radius	13 mm	G Gravity	0.86 N

the estimation process of using HMM to find the column position for two different cases, is included in the supplementary material.

D. Estimating the Row Position and EF Magnitude

Table III lists the material properties of the robot that are required for estimating the row position and the magnitude. Since the algorithm uses an iterative approach to find the optimal values and the model was built assuming the robot is in balance, the system starts to estimate the row position and magnitude 1s after setting an actuation input (robot is stable). The parameter χ is set to 1 and the maximum iteration epoch is 10 in (15). In addition, the mean value and the variance of the Gaussian white noise in (13) were set to 0 and 5, respectively.

In testing, the two hundred sets of actuation inputs were commanded to robot and the bar always excited the robot ensuring $\|\Delta P_k\| \geq \vartheta$ (EF always acts). The final estimated row positions

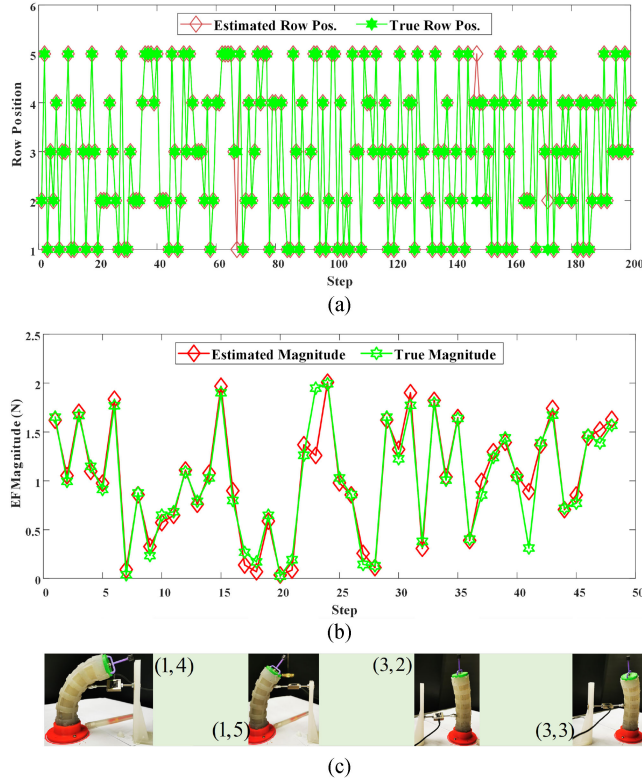


Fig. 8. (a) Row position estimation results. (b) True magnitude and the estimated value. (c) Snapshots of robot disturbed by the force sensor at different area (column position, row position).

and the true ones are illustrated in Fig. 8(a), proving that only 3 (67th, 148th, and 172th) estimated positions failed to meet with the true results, reaching an accuracy of 98.5%.

In terms of validating the magnitude estimation method, the force sensor was mounted at different positions, as Fig. 8(c) shows, which means the position and magnitude of the external force were both known, and then robot was commanded to touch the force sensor, whose output was regarded as the ground truth for validation. The force sensor was fixed beside the four columns of the manipulator, and different actuation inputs were set to command the manipulator to contact the force sensor while the row position was also changed at each column position by manually adjusting the height of the force sensor. In this way, 16 regions on the manipulator surface were tested by the force sensor, and three actuation inputs were considered for each region to set different magnitudes. The row position calculation was based on the results from the column position estimation, which means θ_f can be obtained for further calculation. The estimated results are illustrated in Fig. 8(b). During all the 48 steps, only two (23th and 41th) estimated positions were deviated from the true value, which mainly resulted from the inaccurate row position. As for the magnitude, a maximum force of 2 N was applied for testing, and the maximum error happened on the inaccurate step is 0.71 N, which is caused by the inaccurate estimation of the row position. Other than that, the mean error of the estimated magnitude in other 46 steps is 0.23 N, showing this estimation method combining virtual work principle and regularization algorithm is effective.

The time consumption in estimating the presence of an EF (machine learning), finding the column position (HMM), and solving the row position and the magnitude (virtual work principle) are 0.078, 0.008, and 0.85 s, respectively. The third item is more time-consuming due to the iteration process and the process started after the robot was stable, which would take a longer time. The first and the second items took less time and they can be evaluated in real-time. In addition, the probability model requires fewer data in training.

V. CONCLUSION

Finding the external force acting on a soft robot is important in the field. While majority of work focused on the effect at the end-effector, this article presented a new method to estimate an unknown force acting on the circumferential surface of a continuum robot. The robot was fabricated with integrated eGaIn sensors to provide useful information related to the shape of the robot. This proprioceptive sensing mechanism can eliminate the use of common external measurement devices, allowing the robot to operate in a confined and occluded environment. A model-free approach based on artificial neural network was employed to predict the tip position based on the sensor information, and compared with the tip position under a load-free scenario so that the presence of an external force can then be determined. To find the exact location of the force, the circumferential body of the robot was represented by a 2-D map, and the indices of the map were evaluated accordingly. HMM was employed to find the column position, and the principle of virtual work with a regularization term was used to find the row position and the magnitude. Experimental results confirmed that the model-free approach can predict the tip position with an error of about 4 mm. Different scenarios, including different weights of load, multiple loads, and load-free were examined to ensure the robustness of the prediction method. Random force was exerted onto the robot and this algorithm can achieve an accuracy of 97% and 98.5% in finding the column and row positions, respectively. The error in finding the force magnitude is 0.23 N. This proprioceptive sensing and evaluation algorithms enable the robot to easily sense the force information, allowing better interaction with the surrounding environment.

APPENDIX

The parameters ψ_k , θ_k , and R_k under the tip position $P_k = (x_k, y_k, z_k)$ can be solved by

$$\begin{aligned} \psi_k &= \text{atan2}(y_k, x_k), \theta_k = 2\text{acos}\left(\frac{z_k}{\sqrt{x_k^2 + y_k^2 + z_k^2}}\right), R_k \\ &= l/\theta_k. \end{aligned} \quad (\text{A1})$$

The length of each chamber is

$$l_{k,1} = l(1 - (\theta_k/l)r \cos(\psi_k))$$

$$l_{k,2} = l\left(1 - (\theta_k/l)r \cos\left(\psi_k + \frac{2}{3}\pi\right)\right)$$

$$l_{k,3} = l \left(1 - (\theta_k/l) r \cos \left(\psi_k + \frac{4}{3}\pi \right) \right). \quad (\text{A2})$$

The centroid of the manipulator is

$$C_k = \frac{l}{\theta_k} \left[(1 - \cos \frac{\theta_k}{2}) \cos \psi_k, (1 - \cos \frac{\theta_k}{2}) \sin \psi_k, \sin \frac{\theta_k}{2} \right]^T. \quad (\text{A3})$$

The tip position change due to an UEF is calculated as

$$H_e(m_k)F_{e,k} = \text{rotz}(\theta_f) \begin{bmatrix} \frac{F_{e,k}h(m_k)^2(3l-h(m_k))}{6EI} \\ 0 \\ \frac{2EI}{F_{e,k}h(m_k)^2} \sin\left(\frac{F_{e,k}h(m_k)^2}{2EI}\right) \end{bmatrix}$$

$$\theta_f = \frac{2\hat{n}_k - 1}{4}\pi(\hat{n}_k \neq 5) \quad (\text{A4})$$

where $\text{rotz}(\theta_f)$ denotes a rotation matrix around Z -axis to θ_f , as shown in Fig. 2, and θ_f is involved in the estimated column position.

REFERENCES

- [1] A. Gao, J. Li, Y. Zhou, Z. Wang, and H. Liu, "Modeling and task-oriented optimization of contact-aided continuum robots," *IEEE/ASME Trans. Mechatronics*, vol. 25, no. 3, pp. 1444–1455, Jun. 2020.
- [2] M. F. Rox *et al.*, "Mechatronic design of a two-arm concentric tube robot system for rigid neuroendoscopy," *IEEE/ASME Trans. Mechatronics*, vol. 25, no. 3, pp. 1432–1443, Jun. 2020.
- [3] Q. Wu, X. Wang, B. Chen, H. Wu, and Z. Shao, "Development and hybrid force/position control of a compliant rescue manipulator," *Mechatronics*, vol. 46, pp. 143–153, 2017.
- [4] M. Wang, X. Dong, W. Ba, A. Mohammad, D. Axinte, and A. Norton, "Design, modelling and validation of a novel extra slender continuum robot for in-situ inspection and repair in aeroengine," *Robot. Comput.-Integr. Manuf.*, vol. 67, 2020, Art. no. 102054.
- [5] T. K. Morimoto and A. M. Okamura, "Design of 3-D printed concentric tube robots," *IEEE Trans. Robot.*, vol. 32, no. 6, pp. 1419–1430, Dec. 2016.
- [6] E. B. Joyee and Y. Pan, "A fully three-dimensional printed inchworm-inspired soft robot with magnetic actuation," *Soft Robot.*, vol. 6, no. 3, pp. 333–345, 2019.
- [7] H. C. Fu *et al.*, "Interfacing soft and hard: A spring reinforced actuator," *Soft Robot.*, vol. 7, no. 1, pp. 44–58, 2020.
- [8] F. Xu, H. Wang, Z. Liu, and W. Chen, "Adaptive visual servoing for an underwater soft robot considering refraction effects," *IEEE Trans. Ind. Electron.*, vol. 67, no. 12, pp. 10575–10586, Dec. 2020.
- [9] R. Xu, A. Yurkewich, and R. V. Patel, "Curvature, torsion, and force sensing in continuum robots using helically wrapped FBG sensors," *IEEE Trans. Robot. Autom.*, vol. 1, no. 2, pp. 1052–1059, Jul. 2016.
- [10] S. Song, Z. Li, M. Q.-H. Meng, H. Yu, and H. Ren, "Real-time shape estimation for wire-driven flexible robots with multiple bending sections based on quadratic Bézier curves," *IEEE Sensors J.*, vol. 15, no. 11, pp. 6326–6334, Nov. 2015.
- [11] H. Yang, M. Xu, W. Li, and S. Zhang, "Design and implementation of a soft robotic arm driven by SMA coils," *IEEE Trans. Ind. Electron.*, vol. 66, no. 8, pp. 6108–6116, Aug. 2019.
- [12] H. Zhao, K. O'Brien, S. Li, and R. F. Shepherd, "Optoelectronically innervated soft prosthetic hand via stretchable optical waveguides," *Sci. Robot.*, vol. 1, no. 1, pp. 1–10, 2016.
- [13] R. B. N. Scharff, R. M. Doornbusch, E. L. Doubrovski, J. Wu, J. M. P. Geraedts, and C. C. L. Wang, "Color-based proprioception of soft actuators interacting with objects," *IEEE/ASME Trans. Mechatronics*, vol. 24, no. 5, pp. 1964–1973, Oct. 2019.
- [14] G. Rizzello, P. Serafino, D. Naso, and S. Seelecke, "Towards sensorless soft robotics: Self-sensing stiffness control of dielectric elastomer actuators," *IEEE Trans. Robot.*, vol. 36, no. 1, pp. 174–188, Feb. 2020.
- [15] S. Mikogai, B. D. C. Kazumi, and K. Takemura, "Contact point estimation along air tube based on acoustic sensing of pneumatic system noise," *IEEE Trans. Robot. Autom.*, vol. 5, no. 3, pp. 4618–4625, Jul. 2020.
- [16] J. Zhou, Y. Chen, X. Chen, Z. Wang, Y. Li, and Y. Liu, "A proprioceptive bellows (PB) actuator with position feedback and force estimation," *IEEE Trans. Robot. Autom.*, vol. 5, no. 2, pp. 1867–1874, Apr. 2020.
- [17] J. Tapia, E. Knoop, M. Mutný, M. A. Otaduy, and M. Bächer, "MakeSense: Automated sensor design for proprioceptive soft robots," *Soft Robot.*, vol. 7, no. 3, pp. 332–345, 2020.
- [18] A. Zatopa, S. Walker, and Y. Menguc, "Fully soft 3D-printed electroactive fluidic valve for soft hydraulic robots," *Soft Robot.*, vol. 5, no. 3, pp. 258–271, 2018.
- [19] J.-B. Chossat, Y.-L. Park, R. J. Wood, and V. Duchaine, "A soft strain sensor based on ionic and metal liquids," *IEEE Sensors J.*, vol. 13, no. 9, pp. 3405–3414, Sep. 2013.
- [20] V. Arabagi, O. Felfoul, A. H. Gosline, R. J. Wood, and P. E. Dupont, "Biocompatible pressure sensing skins for minimally invasive surgical instruments," *IEEE Sensors J.*, vol. 16, no. 5, pp. 1294–1303, Mar. 2016.
- [21] A. Al-Azzawi, A. M. Boudali, H. Kong, A. H. Göktogan, and S. Sukkarieh, "Modelling of uniaxial EGain-based strain sensors for proprioceptive sensing of soft robots," in *Proc. IEEE/RSJ Int. Conf. Intell. Robots Syst.*, 2019, pp. 7474–7480.
- [22] J. Avery, M. Runciman, A. Darzi, and G. P. Mylonas, "Shape sensing of variable stiffness soft robots using electrical impedance tomography," in *Proc. Int. Conf. Robot. Automat.*, 2019, pp. 9066–9072.
- [23] C. Tutcu, B. A. Baydere, S. K. Talas, and E. Samur, "Quasi-static modeling of a novel growing soft-continuum robot," *Int. J. Robot. Res.*, vol. 40, no. 1, pp. 86–98, 2021.
- [24] B. Gorissen, D. Reynaerts, S. Konishi, K. Yoshida, J. W. Kim, and M. De Volder, "Elastic inflatable actuators for soft robotic applications," *Adv. Mater.*, vol. 29, no. 43, pp. 1–14, 2017.
- [25] N. Tan, M. Huang, P. Yu, and T. Wang, "Neural-dynamics-enabled Jacobian inversion for model-based kinematic control of multi-section continuum manipulators," *Appl. Soft Comput.*, vol. 103, 2021, Art. no. 107114.
- [26] M. Giorelli, F. Renda, M. Calisti, A. Arienti, G. Ferri, and C. Laschi, "Neural network and jacobian method for solving the inverse statics of a cable-driven soft arm with nonconstant curvature," *IEEE Trans. Robot.*, vol. 31, no. 4, pp. 823–834, Aug. 2015.
- [27] P. Qi, C. Liu, A. Ataka, H. K. Lam, and K. Althoefer, "Kinematic control of continuum manipulators using a fuzzy-model-based approach," *IEEE Trans. Ind. Electron.*, vol. 63, no. 8, pp. 5022–5035, Aug. 2016.
- [28] Y. Chen, L. Wang, K. Galloway, I. Godage, N. Simaan, and E. Barth, "Modal-based kinematics and contact detection of soft robots," *Soft Robot.*, vol. 8, no. 3, pp. 298–309, 2021.
- [29] C. B. Black, J. Till, and D. C. Rucker, "Parallel continuum robots: Modeling, analysis, and actuation-based force sensing," *IEEE Trans. Robot.*, vol. 34, no. 1, pp. 29–47, Feb. 2018.
- [30] I. M. Van Meerbeek, C. M. De Sa, and R. F. Shepherd, "Soft optoelectronic sensory foams with proprioception," *Sci. Robot.*, vol. 3, no. 24, p. eaau2489, 2018, doi: [10.1126/scirobotics.aau2489](https://doi.org/10.1126/scirobotics.aau2489).
- [31] Q. Qiao, D. Willems, G. Borghezan, M. Ourak, J. De Schutter, and E. V. Poorten, "Estimating and localizing external forces applied on flexible instruments by shape sensing," in *Proc. 19th Int. Conf. Adv. Robot.*, 2019, pp. 227–233.
- [32] V. K. Venkiteswaran, J. Sikorski, and S. Misra, "Shape and contact force estimation of continuum manipulators using pseudo rigid body models," *Mechanism Mach. Theory*, vol. 139, pp. 34–45, 2019.
- [33] T. G. Thuruthel, B. Shih, C. Laschi, and M. T. Tolley, "Soft robot perception using embedded soft sensors and recurrent neural networks," *Sci. Robot.*, vol. 4, no. 26, 2019, Art. no. eaav1488.
- [34] E. Bayraktar, C. B. Yigit, and P. Boyraz, "Object manipulation with a variable-stiffness robotic mechanism using deep neural networks for visual semantics and load estimation," *Neural Comput. Appl.*, vol. 32, no. 13, pp. 9029–9045, 2020.
- [35] B. Xiao *et al.*, "Depth estimation of hard inclusions in soft tissue by autonomous robotic palpation using deep recurrent neural network," *IEEE Trans. Automat. Sci. Eng.*, vol. 17, no. 4, pp. 1791–1799, Oct. 2020.
- [36] R. L. Truby, C. D. Santina, and D. Rus, "Distributed proprioception of 3D configuration in soft, sensorized robots via deep learning," *IEEE Trans. Robot. Autom.*, vol. 5, no. 2, pp. 3299–3306, Apr. 2020.
- [37] L. O. Tiziani and F. L. Hammond, "Optical sensor-embedded pneumatic artificial muscle for position and force estimation," *Soft Robot.*, vol. 7, no. 4, pp. 462–477, 2020.

- [38] S. Sun, X. Wang, B. Moran, and W. S. Rowe, "A hidden semi-Markov model for indoor radio source localization using received signal strength," *Signal Process.*, vol. 166, 2020, Art. no. 107230.
- [39] X. Tong *et al.*, "A double-step unscented Kalman filter and HMM-based zero-velocity update for pedestrian dead reckoning using MEMS sensors," *IEEE Trans. Ind. Electron.*, vol. 67, no. 1, pp. 581–591, Jan. 2020.